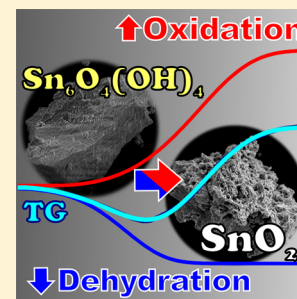


Thermal Decomposition of Tin(II) Oxyhydroxide and Subsequent Oxidation in Air: Kinetic Deconvolution of Overlapping Heterogeneous Processes

Suguru Kitabayashi and Nobuyoshi Koga*

Department of Science Education, Graduate School of Education, Hiroshima University, 1-1-1 Kagamiyama, Higashi-Hiroshima 739-8524, Japan

ABSTRACT: The reaction pathway and mechanistic features of the synthesis of SnO_2 via the oxidative decomposition of tin(II) oxyhydroxide in air were investigated using thermoanalytical techniques and morphological observations. Furthermore, the detailed kinetics of each component process were analyzed by applying an empirical kinetic deconvolution method. The thermal behavior of tin(II) oxyhydroxide in air is characterized by two overall processes: (1) the mass-change process, which involves thermal decomposition (mass loss) and in situ oxidation (mass gain), followed by (2) crystal growth of the product SnO_2 . The mass-change process comprises largely overlapping consecutive processes such as primary endothermic thermal decomposition and subsequent exothermic oxidation. It was deduced from the kinetic results that the overall mass-change process is regulated by the overlapping structures of the surface product layers of the primary and subsequent reactions and the counter diffusion of the H_2O generated in the primary reaction and the reactant O_2 required for the subsequent reaction in the outer layer. The crystal growth of the as-produced SnO_2 occurs via two concurrent kinetic processes that result in the development of a two-dimensional stacking structure. These kinetic features are the key to controlling the overall reaction process and the morphology of the SnO_2 product.



1. INTRODUCTION

Various synthetic methods for the preparation of morphologically controlled SnO_2 have been examined with the objective of identifying additional sophisticated functional properties of this *n*-type wide-bandgap semiconductor^{1,2} that will enable other potential applications, such as gas sensors,^{3–9} anode materials for lithium-ion batteries,^{10–16} transparent thin-film electrodes,^{17–20} optoelectronic devices,^{21–26} and photocatalysts.^{27,28} The majority of these synthetic methods are wet-chemical processes, sometimes facilitated by sol–gel,²¹ hydrothermal,^{6,12,13,15,16,22–24,27,29} microwave-assisted,²⁹ sonochemical processing,¹¹ dip-coating,¹⁷ and spray pyrolysis techniques.^{18,19} The traditional solid-state synthesis method, which involves the thermal decomposition and oxidation of a precursor Sn(II) compound in an oxygen-rich atmosphere, also remains worthwhile as a cost-effective, large-scale process. For example, the oxidative decomposition of crystalline SnC_2O_4 has been examined as a possible synthesis method for nanosized and microstructural SnO_2 ,^{4,30–38} including porous nanorods,^{30,31,37} whiskers,³² and flowerlike and hierarchical constitutions.^{4,33}

However, controlled synthesis of SnO_2 via oxidative decomposition of Sn(II) compounds is challenging. The overall reaction is a complex heterogeneous process involving several interrelated kinetic processes, including thermal decomposition of the precursor, oxidation of the intermediate Sn(II) compound, and crystal growth of SnO_2 , as is observed for many solid-state reactions.^{39–41} The kinetic behavior of each component process and the interrelationships among the processes change depending on the sample and reaction conditions, resulting in different morphological characteristics

and functional properties of the as-produced SnO_2 . In this situation, in addition to knowledge about the empirical preparation–outcome relationship, a detailed understanding of the physico-geometrical reaction mechanism of each component process and their mutual correlations that characterize the overall reaction kinetics is necessary to enable the strategic design of controlled SnO_2 synthesis. Previously,⁴² the present authors investigated the physico-geometrical mechanisms and overall kinetics of the oxidative decomposition of SnC_2O_4 in flowing air using thermoanalytical techniques and morphological observations. It was clarified that the reaction proceeds in a shrinking core regime composed of overlapping multistep kinetic processes in which the gaseous diffusion of both the byproduct and reactant through the surface product layer of SnO_2 regulates the overall kinetics. In a particular case, the overall reaction advanced with the intermittent reaction behavior induced by the formation of pores and cracks in the surface product layer. Therefore, the overall reaction pathway and kinetics are largely regulated by the self-generated geometric constitutions and reaction conditions that result in the formation of two-dimensional SnO_2 architectures. These findings for the oxidative decomposition well illustrate the importance of understanding both the mechanisms and kinetics of the synthetic reactions involved in solid-state processes.

Tin(II) oxyhydroxide, $\text{Sn}_6\text{O}_4(\text{OH})_4$, is an alternative precursor for SnO_2 synthesis via solid-state oxidative

Received: May 25, 2015

Revised: June 21, 2015

Published: June 22, 2015

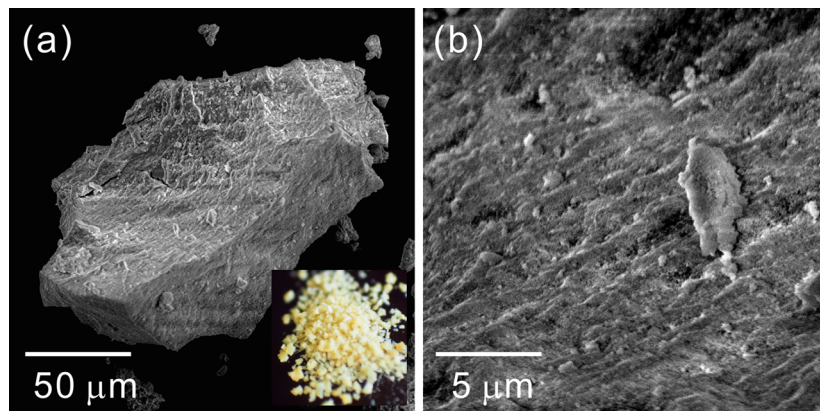


Figure 1. Microscopic views of prepared $\text{Sn}_6\text{O}_4(\text{OH})_4 \cdot n\text{H}_2\text{O}$ sample: (a) SEM image and optical microscopic view (insert) and (b) surface texture.

decomposition.^{43,44} Recently, Wang et al. reported the formation of differently sized hierarchical SnO_2 octahedra composed of nanoparticles (30–40 nm in diameter) via the calcination of $\text{Sn}_6\text{O}_4(\text{OH})_4$ (precipitated using a sonochemical technique) at 1073 K for 3 h in air.⁴³ The successful controlled synthesis of microstructural SnO_2 stimulated our interest in investigating the mechanistic and kinetic details of the thermal decomposition and oxidation of $\text{Sn}_6\text{O}_4(\text{OH})_4$ to achieve further control of the synthetic process. As the first part of a series of kinetic studies of this reaction, the thermal behavior of poorly crystalline $\text{Sn}_6\text{O}_4(\text{OH})_4$ precipitated in aqueous media without the addition of organic compounds is reported herein. The largely overlapping mass-loss and mass-gain processes ascribed to thermal decomposition and the subsequent oxidation, respectively, were separately characterized using an empirical kinetic deconvolution method.⁴⁵ The crystal growth of as-produced SnO_2 via the thermal decomposition and oxidation of $\text{Sn}_6\text{O}_4(\text{OH})_4$ was also subjected to kinetic analysis. Based on the results of these kinetic studies and the morphological observations, the mechanistic features of the reaction that are closely related to the formation of structural SnO_2 are discussed.

2. EXPERIMENTAL SECTION

2.1. Sample Preparation and Characterization. Stock solutions of 0.10 M $\text{SnCl}_2(\text{aq})$ and 0.10 M $\text{NaOH}(\text{aq})$ were prepared by dissolving $\text{SnCl}_2 \cdot 2\text{H}_2\text{O}(\text{s})$ (>99.7%, Nacalai Tesque) into 0.10 M $\text{HCl}(\text{aq})$ (>98%, Sigma-Aldrich Japan) and by dissolving $\text{NaOH}(\text{s})$ (>98%, Sigma-Aldrich Japan) into deionized and distilled water, respectively. With mechanical stirring using a magnetic stirrer in the ambient atmosphere, 100 cm^3 of the $\text{SnCl}_2-\text{HCl}(\text{aq})$ stock solution was titrated using the $\text{NaOH}(\text{aq})$ stock solution at a rate of approximately 10 $\text{cm}^3 \text{ min}^{-1}$ until the total $\text{NaOH}(\text{aq})$ volume reached 300 cm^3 . The obtained $\text{Sn}_6\text{O}_4(\text{OH})_4$ precipitates were separated by vacuum filtration and were carefully rinsed using deionized-distilled water until the filtrate was free from chloride ions. The separated precipitates were dried in a vacuum desiccator at room temperature for 24 h and stored in a refrigerator at 278 K. Prior to each experiment, a sample was gently crushed using an agate mortar and pestle and then sieved (100–200 mesh) to provide a fraction containing 75–150 μm particles.

The powder X-ray diffraction (XRD) pattern of the sample was recorded using a diffractometer (RINT2200 V, Rigaku, 40 kV, 30 mA, 4° min^{-1}). Fourier transform infrared (FT-IR) spectra were obtained using a spectrophotometer (FT-IR8400s,

Shimadzu) and the diffuse reflectance method after diluting the sample with KBr. The appearance and morphology of the sample were observed using an optical microscope (SZX7, Olympus) and a scanning electron microscopy instrument (SEM; JSM-6510, JEOL) after coating the $\text{Sn}_6\text{O}_4(\text{OH})_4$ particles with Pt via sputtering (JFC-1600, JEOL; 30 mA, 90 s), respectively.

2.2. Measurement of Thermal Behavior. Simultaneous thermogravimetry–differential thermal analysis (TG–DTA; TG8120, Rigaku) measurement for 5.0 mg of the sample, weighed into a platinum pan (5 mm in diameter and 2.5 mm in height), was performed at a heating rate, β , of 10 K min^{-1} in a flow of a mixed $\text{He}-\text{O}_2$ gas (21% O_2) at a rate of 200 $\text{cm}^3 \text{ min}^{-1}$. During the measurement, a portion of the outlet gas from the heating chamber of the TG–DTA instruments was continuously introduced into a quadrupole mass spectrometry instrument (MS; M-200Q, Anerva) through a silica capillary tube (0.075 mm internal diameter) heated at 500 K. The MS spectra of the evolved gases were repeatedly recorded in the range from 10 to 50 amu (EMSN, 1.0 A; SEM, 1.0 kV) every 5 s.

The sample was fitted to a platinum plate by pressing and subjected to high temperature XRD measurements at different temperatures in the range of 323–973 K in steps of 50 K. The measurements were performed using an RINT2200 V equipped with a programmable heating chamber (PTC-20A, Rigaku). The sample fitted to a platinum plate was heated in flowing air ($100 \text{ cm}^3 \text{ min}^{-1}$) in a stepwise isothermal manner at a heating rate of 10 K min^{-1} and was maintained at different selected temperatures for 15 min during each diffraction measurement under the conditions described above.

Samples of 5.0 mg, weighed into a platinum pan (6 mm in diameter and 2.5 mm in height), were heated to different temperatures (413, 483, 533, 573, 673, and 753 K) at a β (10 K min^{-1}) in flowing air ($80 \text{ cm}^3 \text{ min}^{-1}$) using a top-loading type TG–DTA instrument (DTG50, Shimadzu). The heat-treated samples were immediately cooled to room temperature and subjected to microscopic observations (optical microscope and SEM). TG–DTA curves of the sample were also obtained under the same measurement conditions but with heating at different β ($1.0 \leq \beta \leq 10.0 \text{ K min}^{-1}$) from room temperature to 823 K to record the kinetic rate data for thermal decomposition and oxidation of the decomposition product. Differential scanning calorimetry (DSC; DSC60, Shimadzu) measurements were also performed under the same measurement conditions as those used for the TG–DTA measurements, but at different

β ($2.0 \leq \beta \leq 10.0 \text{ K min}^{-1}$), to record the kinetic rate data for crystal growth of the oxidation product. Through systematic preliminary measurements under different measurement conditions, the measurement conditions of the TG–DTA and DSC for recording the kinetic rate data were selected and the reliability and repeatability of the thermoanalytical data as the kinetic rate data under the selected measurement conditions were confirmed. In the preliminary experiments, it was experienced that when the thermoanalytical measurements in air were performed using the smaller agglomerates of $\text{Sn}_6\text{O}_4(\text{OH})_4$ and larger sample masses at higher heating rates, the reaction exhibited thermal runaway behavior due to the significant exothermic effect of the oxidation process, resulting in flying apart of the samples from the sample crucible due to the rapid escape of H_2O generated during thermal decomposition.

3. RESULTS AND DISCUSSION

3.1. Sample Characterization. Figure 1 shows typical views of a prepared sample. The sample was pale yellow, and agglomerates with diameter of approximately $100 \mu\text{m}$ exhibited a dried gel-like appearance (Figure 1a and insert) with a stacking structure (Figure 1b). The XRD pattern and FT-IR spectrum of the sample are shown in Figure 2. Weak peaks in

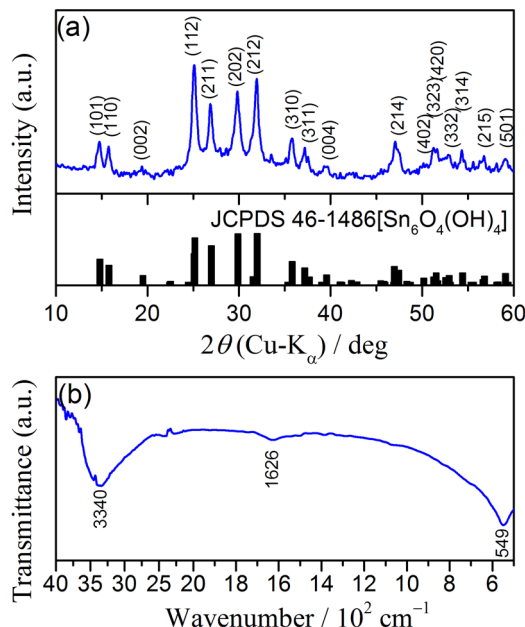


Figure 2. Characterization of prepared $\text{Sn}_6\text{O}_4(\text{OH})_4 \cdot n\text{H}_2\text{O}$ sample: (a) XRD pattern and (b) FT-IR spectrum.

the XRD pattern (Figure 2a) indicate a poorly crystalline nature, but the pattern agrees well with that of $\text{Sn}_6\text{O}_4(\text{OH})_4$ (space group, $P\bar{4}2_1c$; $a = 7.92680 \text{ \AA}$, $c = 9.10250 \text{ \AA}$; JCPDS entry 46-1486).⁴⁶ The FT-IR spectrum (Figure 2b) shows the O–H stretching and Sn–O stretching bands at 3340 and 549 cm^{-1} , respectively, in agreement with the reported spectrum of $\text{Sn}_6\text{O}_4(\text{OH})_4$.^{44,47} The absorption peak at 1626 cm^{-1} was ascribed to the H–O–H bending, indicating the possible presence of water molecules in the agglomerated sample. Therefore, the sample composition was provisionally expressed as $\text{Sn}_6\text{O}_4(\text{OH})_4 \cdot n\text{H}_2\text{O}$.

3.2. Thermal behavior. Figure 3 shows typical TG–derivative TG (DTG)–DTA curves for the sample that were

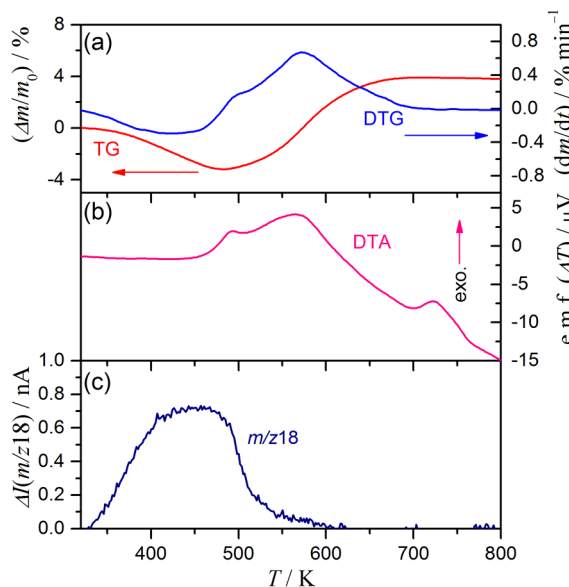
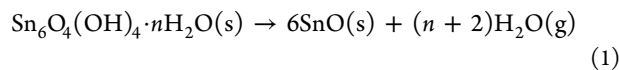
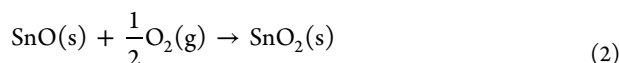


Figure 3. Thermoanalytical curves for prepared $\text{Sn}_6\text{O}_4(\text{OH})_4 \cdot n\text{H}_2\text{O}$ sample ($m_0 = 5.0 \text{ mg}$) recorded in flowing He–O₂ (21% O₂, $200 \text{ cm}^3 \text{ min}^{-1}$) with heating at $\beta = 10 \text{ K min}^{-1}$: (a) TG–DTG curves, (b) DTA curve, and (c) mass chromatogram ($m/z = 18$) of evolved gas.

recorded in a flowing He–O₂ mixture (21% O₂, $200 \text{ cm}^3 \text{ min}^{-1}$), together with the mass chromatogram for H₂O⁺ ($m/z = 18$) in the outlet gas from the TG–DTA instruments. The mass-change trace initially exhibits a mass loss followed by a mass gain before reaching a constant mass at approximately 700 K. The mass loss was attributed to the thermal dehydration–decomposition of $\text{Sn}_6\text{O}_4(\text{OH})_4 \cdot n\text{H}_2\text{O}$ to form SnO:⁴⁸



Dehydration of the crystalline or bound water and thermal decomposition of hydroxide cannot be distinguished in the smooth TG curve representing the mass-loss process. Furthermore, the minimum sample mass reached during the measurement is notably larger than the expected value assuming the stoichiometric formation of SnO(s). At the flexion point of the DTG curve during the mass-loss process (approximately 450 K), the DTA curve begins to shift to the exothermic direction. The exothermic behavior continues until the end of the mass-gain process with a maximum of the DTA exothermic peak at approximately 575 K, which occurs after a smaller exothermic peak at the point corresponding to the mass-loss–mass-gain inflection point in the TG curve. This mass-gain process accompanied by an exothermic effect was attributed to the thermally induced oxidation of the as-produced SnO(s):⁴⁹



During the mass-change process, only H₂O is clearly detected in the mass spectra of the evolved gases, as can be seen in the mass chromatogram for H₂O⁺ ($m/z = 18$) (Figure 3c). Furthermore, the evolution of H₂O continues even after the mass-change curve switches from a mass loss to a mass gain. This result indicates that the thermal dehydration–decomposition of $\text{Sn}_6\text{O}_4(\text{OH})_4 \cdot n\text{H}_2\text{O}$ and the thermally induced oxidation of the as-produced SnO partially overlapped. From the relative mass change in the sample during the entire mass-

change process to form SnO_2 (eqs 1 and 2), the n value in $\text{Sn}_6\text{O}_4(\text{OH})_4 \cdot n\text{H}_2\text{O}$ was calculated to be 1.5. Furthermore, after completion of the mass-change process, a distinguishable exothermic peak is observed in the temperature range from 700 to 800 K, possibly suggesting the growth of SnO_2 crystallites.

Figure 4 illustrates the analytical results for the crystalline phase changes during heating of the prepared $\text{Sn}_6\text{O}_4(\text{OH})_4$.

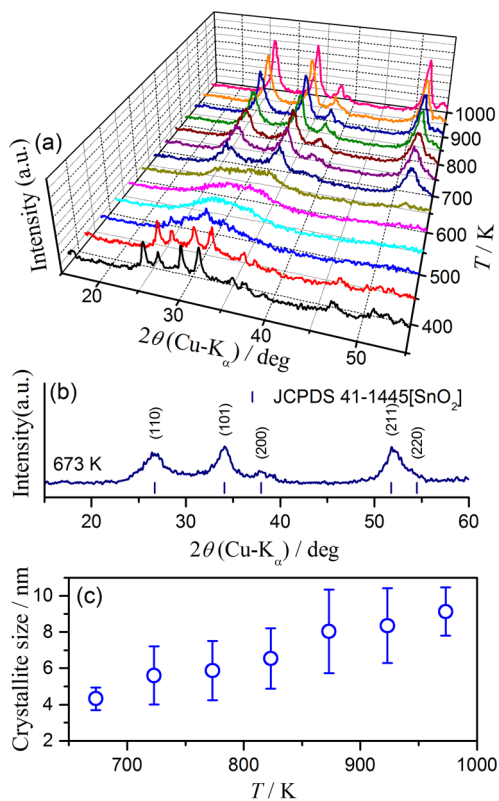


Figure 4. Changes in crystalline phase during heating of prepared $\text{Sn}_6\text{O}_4(\text{OH})_4 \cdot n\text{H}_2\text{O}$ sample in flowing air ($100 \text{ cm}^3 \text{ min}^{-1}$): (a) changes in XRD pattern of sample with temperature, (b) XRD pattern at 673 K, and (c) changes in crystallite size of SnO_2 estimated from diffraction peaks using Scherrer's equation.

$n\text{H}_2\text{O}$ sample in air. When the sample is heated in a stepwise isothermal manner (Figure 4a), the diffraction peaks for $\text{Sn}_6\text{O}_4(\text{OH})_4$ gradually diminish, indicating the formation of an even less crystalline phase at 500 K, which corresponds to the inflection point in the mass-change trace from mass loss to mass gain. The diffraction peaks for the final product begin to grow at 623 K, and the XRD pattern (Figure 4b) is in good agreement with that of SnO_2 (tetragonal rutile; space group, $P4_2/mnm$; $a = b = 4.738 \text{ \AA}$, $c = 3.187 \text{ \AA}$; JCPDS entry 41-1445).⁵⁰ Upon further heating of the product SnO_2 , the intensity of the XRD peaks gradually increases. Using Scherrer's equation⁵¹ with reference to the diffraction peaks indexed by (110), (101), and (211), it was determined that the SnO_2 crystallites grew from $4.3 \pm 0.6 \text{ nm}$ to $9.1 \pm 1.3 \text{ nm}$ during heating of the sample from 673 to 973 K (Figure 4c). Furthermore, the growth of the SnO_2 crystallites mainly occurred at temperatures higher than 700 K; therefore, the DTA exothermic peak observed in the temperature range from 700 to 800 K (Figure 3) can be ascribed to the crystal growth of SnO_2 .

Figure 5 shows optical (Figure 5a) and SEM images (Figure 5b–f) of the samples heated to different temperatures. The sample color changes from pale yellow to orange at 483 K (reflection point from mass loss to mass gain). At this temperature, the agglomerated sample particles are heavily cracked because of the stress and strain introduced by thermal dehydration-decomposition and oxidation of the surface layer. A close correlation between the cracking and the small DTG and DTA exothermic peaks is observed in the corresponding temperature range (Figure 3a,b), indicating temporary acceleration of the overall reaction by the newly cleaved surfaces. At 573 K (the point at which maximum mass gain rate is observed during the mass-change process), the sample is dark brown (Figure 5a) and the surfaces of larger agglomerates possess many pores at the interstices of the aggregates (Figure 5c). The pores were likely produced via the thermal dehydration-decomposition process and served as possible channels for intake of the oxygen required for thermally induced oxidation of the as-produced SnO . At 673 K (the end of the mass-change process), the sample is brown (Figure 5a). The surfaces of the agglomerates still possess nanosized grains and pores. After further heating to 753 K (at the end of the exothermic process observed after the completion of the mass-change process), the sample is pale yellow (Figure 5a). The agglomerated particles are also significantly porous and easily crushed (Figure 5e). Furthermore, the product grains that form the agglomerates (Figure 5f) are larger than those observed in Figure 5d and exhibit a platelike appearance. At the same time, the stacking structure observed for the original reactant agglomerates was maintained and further developed during the thermally induced processes. We previously observed the development of a two-dimensional architecture in the SnO_2 obtained from the oxidative decomposition of tin(II) oxalate,⁴² and such a structure has also been reported for SnO_2 synthesized via different wet-chemical processes.^{16,52}

The thermal dehydration-decomposition of the poorly crystalline and dried gel-like $\text{Sn}_6\text{O}_4(\text{OH})_4 \cdot n\text{H}_2\text{O}$ and oxidation of the as-produced SnO in air occur in different temperature ranges, but with some overlap. Compared to the oxidative decomposition of tin(II) oxalate reported previously,⁴² the thermal dehydration-decomposition to form SnO occurred at lower temperatures, while the thermally induced oxidation of the generated poorly crystalline SnO to form SnO_2 occurred at higher temperatures. Thus, the thermal dehydration-decomposition process of $\text{Sn}_6\text{O}_4(\text{OH})_4 \cdot n\text{H}_2\text{O}$, which is the preliminary process for the subsequent oxidation of SnO , appears to play a role in determining the reaction conditions for SnO oxidation. Cracking of the agglomerate particles and formation of pores on the particle surfaces during the thermal dehydration-decomposition process are the possible factors that regulate the overall kinetic behavior. At the same time, the surface SnO_2 product layer that formed as a result of the subsequent oxidation reaction may significantly influence the internal reactions because the diffusion processes for removal of the H_2O gas that was produced during the thermal dehydration-decomposition and intake of the O_2 that was required for oxidation through the surface product layer are regulated by the characteristics of this layer. Kinetic analysis of the overall reaction and, if possible, each component process, is therefore necessary to characterize the mechanistic features of the reaction.

3.3. Kinetics of Overlapping Thermal Dehydration-Decomposition and Oxidation Processes. Figure 6 shows

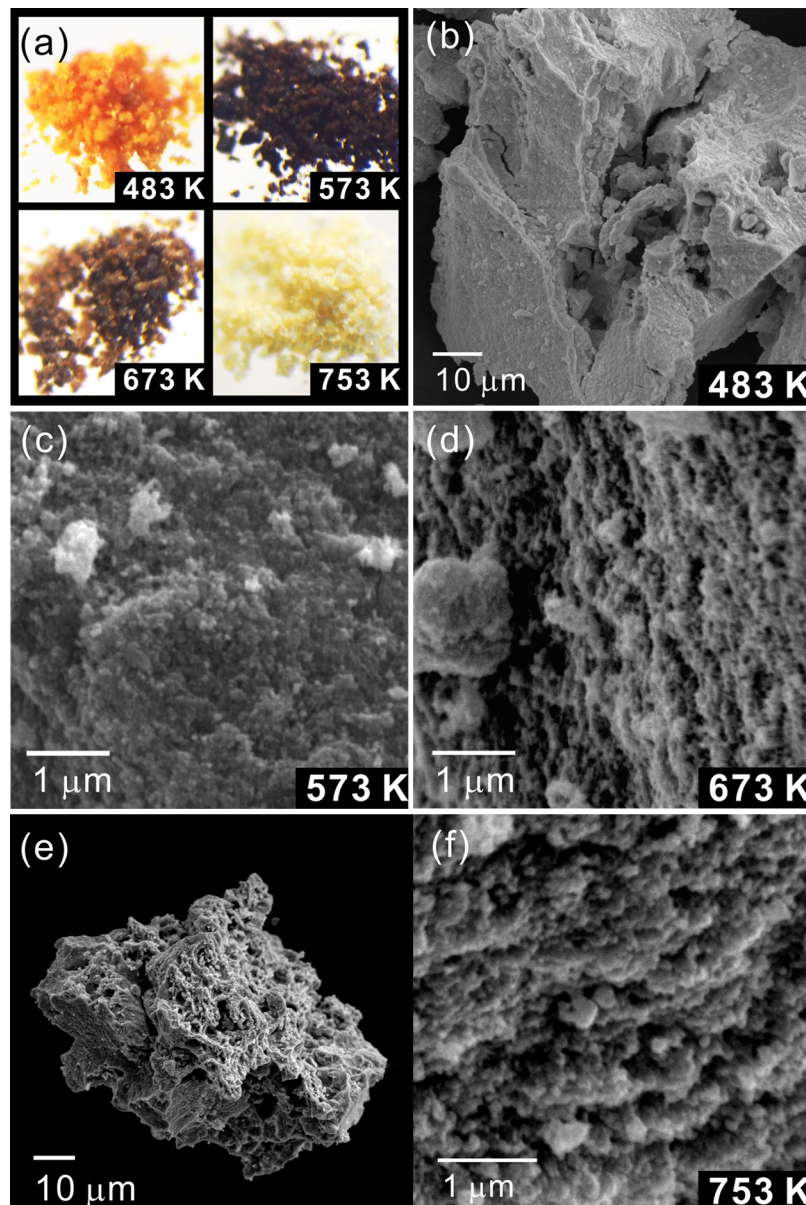


Figure 5. Microscopic views of the samples heated in flowing air ($80 \text{ cm}^3 \text{ min}^{-1}$) to different temperatures at $\beta = 10 \text{ K min}^{-1}$. (a) Optical microscopic images of samples heated to different temperatures; (b–f) SEM images of samples heated to different temperatures: (b) 483 K, (c) 573 K, (d) 673 K, and (e, f) 753 K.

the TG–DTG–DTA curves for the thermal dehydration–decomposition and oxidation processes recorded in flowing air ($80 \text{ cm}^3 \text{ min}^{-1}$) at different β , which were used as the kinetic rate data. Because the thermal dehydration–decomposition and subsequent oxidation of the intermediate product occur simultaneously to some extent, a kinetic understanding of each reaction and their mutual relationship is necessary to determine the overall rate behavior and enable control of the size and morphology of the final SnO_2 product. However, kinetic modeling of the overall process for the formation of SnO_2 with consideration of the mutual relationship between the two chemical processes is extremely difficult; the real heterogeneities of both reaction processes are separated in time and space with certain physico-geometrical restrictions. Furthermore, the different gaseous diffusion processes involved in each reaction (diffusional removal of water vapor in the thermal dehydration–decomposition process and diffusional

uptake of oxygen from the reaction atmosphere in the oxidation process) add further complexity to the overall reaction behavior.⁵³ In this situation, an empirical deconvolution of the overlapping reactions by assuming independent kinetic processes is a possible approach to understanding their individual kinetics,^{42,45,53–66} from which data their mutual relationship may be subsequently considered.⁶⁷

To use this approach, determination of the apparent activation energy, E_a , for each reaction process appears to be the first step. Practically, after finding the characteristic data point related to each reaction process in a series of kinetic rate data at different β , the E_a values for each reaction process can be roughly determined using the isoconversional kinetic relationship,^{68,69} assuming that the single-step approximation is applicable for the selected data points. After various possible ways to apply the isoconversional kinetic approach to the present reaction were examined in view of the most reliable

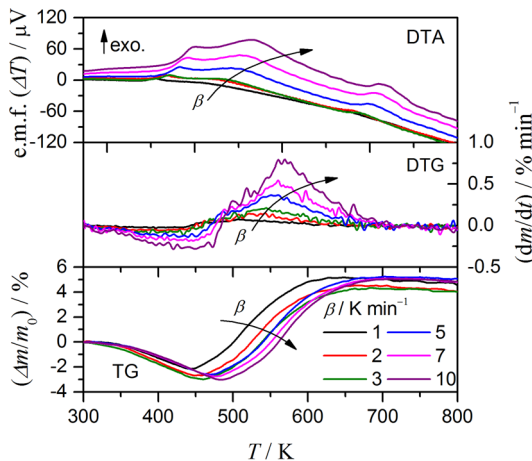


Figure 6. TG–DTG–DTA curves for prepared $\text{Sn}_6\text{O}_4(\text{OH})_4 \cdot n\text{H}_2\text{O}$ sample ($m_0 = 5.0 \text{ mg}$) heated in flowing air ($80 \text{ cm}^3 \text{ min}^{-1}$) at different β .

isoconversional kinetic relationship, the changes in the end set temperatures for the mass loss (thermal dehydration–decomposition) in the TG curves and the peak temperatures for the mass gain (oxidation of intermediate SnO) in the DTG curves as a function of β were referenced to roughly determine the E_a values of the corresponding processes. Assuming a constant degree of conversion for the thermal dehydration–decomposition at the end set for the mass loss in the TG curve irrespective of β , the E_a value was determined using the Ozawa method according to eq 3:^{69,70}

$$\log \beta \cong \log \left[\frac{AE_a}{g(\alpha)R} \right] + a - \frac{bE_a}{RT} \quad (3)$$

where T , A , R , and α are the absolute temperature, Arrhenius preexponential factor, gas constant, and fractional reaction, respectively. The values of a and b are the constants for the approximation of exponential temperature integral ($a = -2.315$ and $b = 0.4567$ within $20 \leq E_a/RT \leq 100$).⁷¹ The function $g(\alpha)$ is the kinetic model function in integral form that describes the physico-geometrical characteristics of the solid-state reactions.

For the mass-gain process, because the peaks of the DTG curves recorded at different β were selected for calculating the E_a value, the Kissinger method was applied to the relationship between β and the peak temperature T_p :⁷²

$$\ln \left(\frac{\beta}{T_p^2} \right) = \ln \left[-\frac{df(\alpha_p)}{d\alpha} \frac{AR}{E_a} \right] - \frac{E_a}{RT_p} \quad (4)$$

where $f(\alpha)$ is the kinetic model function in differential form. Figure 7 shows the Ozawa and Kissinger plots applied to the mass-loss and mass-gain processes, respectively. The plots show sufficient linearity with $R^2 > 0.99$ for the linear regression analyses. From the slopes of the plots, the E_a values for the thermal dehydration–decomposition and oxidation processes were determined to be 93.2 ± 3.2 and $115.1 \pm 4.8 \text{ kJ mol}^{-1}$, respectively.

Assuming partial overlap of the kinetically independent processes, the overall rate behavior can be expressed by the sum of the kinetic equations of the two component processes:^{42,45,53,54,56–60,62–64,66}

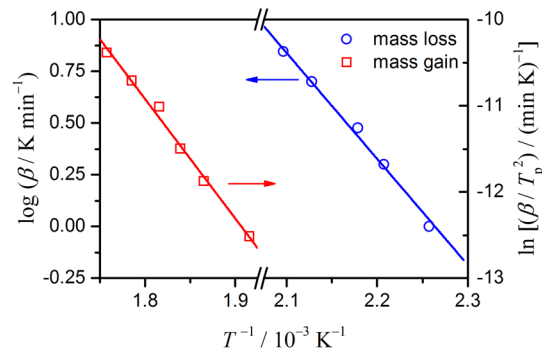


Figure 7. Ozawa and Kissinger plots applied to mass-loss and mass-gain processes, respectively.

$$\frac{d\alpha}{dt} = \sum_{i=1}^2 c_i A_i \exp\left(-\frac{E_{a,i}}{RT}\right) f_i(\alpha_i)$$

with $\sum_{i=1}^2 c_i = 1$ and $\sum_{i=1}^2 c_i \alpha_i = \alpha$ (5)

where c_i , A_i , $E_{a,i}$, α_i , and $f_i(\alpha_i)$ are the contribution, preexponential factor, apparent activation energy, fractional reaction, and kinetic model function in differential form of the reaction process i , respectively. The overall value of α in eq 5 was defined from the overall mass change due to thermal dehydration–decomposition of $\text{Sn}_6\text{O}_4(\text{OH})_4 \cdot n\text{H}_2\text{O}$ and oxidation of the intermediate compound. The contributions of each reaction to the overall mass-change process were then unambiguously determined according to the reaction stoichiometries in eqs 1 and 2 assuming that the amount of water in the sample was $n = 1.5$, that is $(c_1, c_2) = (-1.24, 2.24)$. To obtain the best fit of the mass-change behavior calculated using eq 5 to the experimentally resolved data, an empirical kinetic model function with three kinetic exponents, known as the Šesták–Berggren model (SB(m, n, p): $f(\alpha) = \alpha^m(1 - \alpha)^n[-\ln(1 - \alpha)]^p$)^{73–75} was adopted as the kinetic model function for both reaction processes because the SB(m, n, p) model was sufficiently flexible to accommodate the different types of kinetic behaviors.^{76–79} The E_a values determined by the Ozawa and Kissinger plots (Figure 7) were used as the initial settings for the kinetic parameters for the respective reaction processes. The first-order equation, SB(0, 1, 0), was tentatively assigned to $f_i(\alpha_i)$ for both of the reactions. The order of the initial A_i values was then determined by comparing the overall kinetic rate data obtained experimentally to the theoretical curve drawn according to eq 5.

Optimization of the kinetic parameters, $E_{a,i}$, A_i , m_i , n_i , and p_i was performed to minimize the squared sum of the residuals, F , when fitting the calculated data to the experimental kinetic rate data:

$$F = \sum_{j=1}^M \left[\left(\frac{d\alpha}{dt} \right)_{\text{exp},j} - \left(\frac{d\alpha}{dt} \right)_{\text{cal},j} \right]^2 \quad (6)$$

The results of the kinetic deconvolution analysis, which were determined to gain a separate understanding of each reaction process, are shown in Figure 8. The overall mass-change process was satisfactorily separated into the mass-loss and mass-gain processes (Figure 8a). It can be clearly seen in the figure that 90% of the primary thermal dehydration–decomposition process overlaps the subsequent SnO oxidation process. The

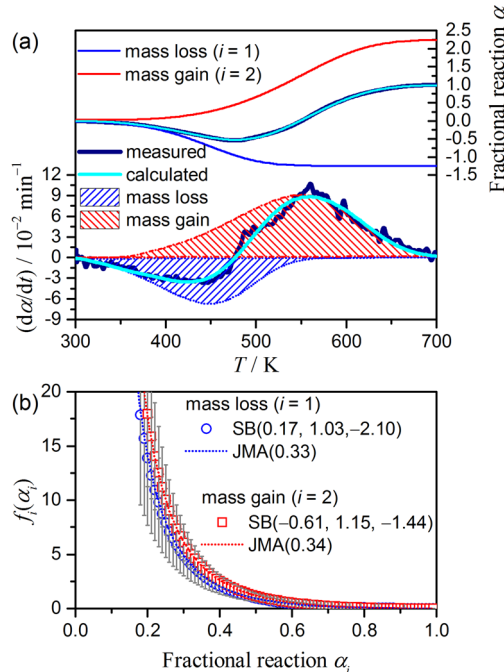


Figure 8. Results of kinetic deconvolution analysis for overall mass-change process: (a) typical results for kinetic rate data at $\beta = 7 \text{ K min}^{-1}$ and (b) experimental master plots of $f_i(\alpha_i)$ versus α_i for mass-loss and mass-gain processes.

rate of the subsequent oxidation process reached a maximum at approximately the end of the thermal dehydration-decomposition process; thus, the second half of the oxidation process advanced as an independent process. Table 1 lists the average calculated kinetic parameters for the respective reaction processes along with those determined for the kinetic rate data at different β . Notably, the optimized $E_{a,i}$ values do not significantly deviate from the initial values determined from the isoconversional relationship among the kinetic rate data at different β . Therefore, the other optimized kinetic parameters, which are constant for the different β as expected from the sufficiently small standard deviations, were interpreted to be the apparent values determined under the fixed $E_{a,i}$ values. The rate behaviors estimated for each reaction are represented by the $SB(m_i, n_i, p_i)$ versus α_i plots^{80,81} in Figure 8b. The rate behaviors for both processes display similar functional dependences on α_i that involve significant decelerating trends. However, these behaviors could not be fitted by any models for diffusion-controlled behavior based on a geometrical scheme. On the other hand, they were superficially fitted by the nucleation and growth-type model, $JMA(m): f(\alpha) = m(1 - \alpha)^{-m}[-\ln(1 - \alpha)]^m$ ^{82–85} but with a small value of $m < 0.5$ that cannot be theoretically explained based on the ideal physico-geometrical model for nucleation and growth mechanisms. The A_i values for the different reactions were also comparable. Therefore, based on these results of the kinetic deconvolution of the overlapping mass-loss and mass-gain processes, it was concluded that the reactions proceeded in similar physico-

geometrical contexts and the difference between the reaction temperature ranges of the respective processes is reflected by the different $E_{a,i}$ values.

The mechanistic features of the overlapping thermal dehydration-decomposition and subsequent SnO_2 oxidation processes were further deduced by combining the results of the morphological observations and kinetic analysis. The reaction begins with the thermal dehydration-decomposition on the surfaces of the agglomerates of the poorly crystalline $\text{Sn}_6\text{O}_4(\text{OH})_4 \cdot n\text{H}_2\text{O}$ (Figure 5b). Because the maximum rate of the mass-loss process occurs at the beginning of the reaction when the reaction at a constant temperature is simulated as seen in the experimental master plot (Figure 8b), it is deduced that the surface process was instantaneously complete and that the reaction geometry immediately became dominated by the contracting volume because of the inward advancement of the reaction interface between the surface product layer and internal solid in the agglomerates. During this process, cracking of the agglomerates was inevitable because of the stress and strain induced by the reaction. The newly cleaved surfaces then reacted immediately, but the contribution of the reaction of the cleaved surfaces to the overall reaction rate could not be effectively estimated because of the significant deceleration of the overall rate of the thermal dehydration-decomposition process. Furthermore, in a contracting volume reaction geometry, the rate decelerates regardless of whether the interfacial reaction is controlled by a chemical reaction or by diffusion. However, the rate behavior of the thermal dehydration-decomposition process could not be described even by diffusion-controlled models with a more significant deceleration trend than those of phase boundary reaction-controlled models. Formation of the SnO_2 surface product layer through initiation of the subsequent oxidation reaction is the most probable cause of the significant deceleration of the thermal dehydration-decomposition process. The subsequent oxidation reaction is also thought to advance via surface reactions and to proceed under the contracting volume scheme. Under these conditions, H_2O produced at the internal reaction interface for thermal dehydration-decomposition is removed from the reaction system through the SnO and SnO_2 product layers. In the region in which the two reaction processes occur simultaneously, the gaseous diffusion through the outer SnO_2 product layer is very complex because the counter-diffusion of H_2O and O_2 is necessary for the advancement of both reactions. The difficulty of O_2 reaching the internal reaction interface for the oxidation reaction may be the cause of the significant deceleration of this reaction (Figure 8b). From the very similar rate behaviors for the thermal dehydration-decomposition and subsequent oxidation processes (Figure 8b), it can be concluded that the diffusional removal of H_2O and diffusional intake of O_2 through the SnO_2 product layer play predominant roles in controlling the overall rates of the largely overlapping reaction processes.

3.4. Kinetics of Tin(IV) Oxide Crystal Growth. In addition to the overlap between the thermal dehydration-decomposition and subsequent oxidation reactions, the crystal

Table 1. Average Kinetic Parameters for Mass-Loss and Mass-Gain Processes at Different β

reaction process	$E_{a,i} (\text{kJ mol}^{-1})$	$A_i (\text{s}^{-1})$	m_i	n_i	p_i
mass loss ($i = 1$)	93.0 ± 1.4	$(9.31 \pm 0.14) \times 10^7$	-0.17 ± 0.06	1.03 ± 0.03	-2.10 ± 0.06
mass gain ($i = 2$)	115.6 ± 0.9	$(9.23 \pm 0.32) \times 10^7$	-0.61 ± 0.03	1.15 ± 0.02	-1.44 ± 0.04

growth of SnO_2 , which occurs along with an exothermic peak after completion of the mass-change process, must be considered with respect to controlling the reaction and the SnO_2 product. Figure 9 shows the results of the formal kinetic

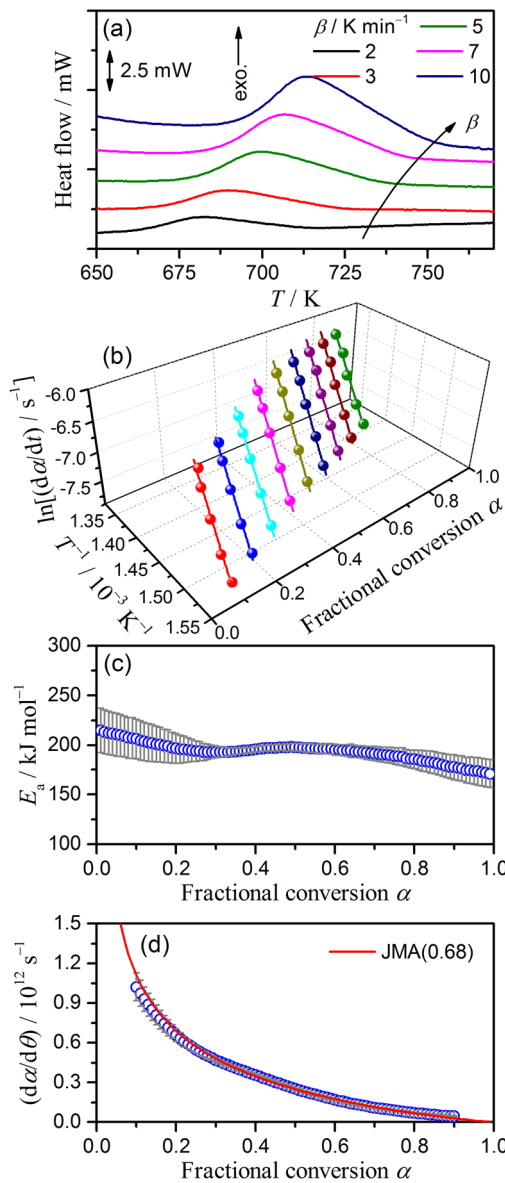


Figure 9. Results of formal kinetic analysis of SnO_2 crystal growth: (a) DSC curves at different β , (b) Friedman plots at different α , (c) apparent E_a values at different α , and (d) experimental master plot and fitting curve using $\text{JMA}(m)$ model.

analysis of the SnO_2 crystal growth using the DSC curves recorded at different β (Figure 9a). The average enthalpy change, ΔH , was determined to be $-24.1 \pm 1.1 \text{ kJ} (\text{mol } \text{SnO}_2)^{-1}$. After the DSC curves are transformed to the kinetic rate data normalized to the fractional conversion, α , with reference to the total ΔH values, the series of kinetic rate data for the crystal growth of SnO_2 at different β were analyzed using the differential isoconversional method known as the Friedman method:^{86,87}

$$\ln\left(\frac{d\alpha}{dt}\right) = \ln[Af(\alpha)] - \frac{E_a}{RT} \quad (7)$$

Plots of $\ln(d\alpha/dt)$ versus T^{-1} at selected α for the kinetic rate data obtained at different β were sufficiently linear irrespective of α (Figure 9b). Although a systematic decrease in the E_a values calculated from the slopes of the Friedman plots at different α was observed in the initial stage of crystal growth ($\alpha \leq 0.3$), the average E_a value for overall crystal growth ($0.10 \leq \alpha \leq 0.90$) was $193.3 \pm 6.0 \text{ kJ mol}^{-1}$ (Figure 9c). The kinetic rate data was then extrapolated to infinite temperature using the isoconversional relationship by assuming that crystal growth occurred via a single-step kinetic process:^{89,70,88}

$$\frac{d\alpha}{d\theta} = \frac{d\alpha}{dt} \exp\left(-\frac{E_a}{RT}\right) \quad \text{with} \quad \theta = \int_0^t \exp\left(-\frac{E_a}{RT}\right) dt \quad (8)$$

where θ is Ozawa's generalized time denoting a hypothetical reaction time at infinite temperature.^{70,89} The plot of $(d\alpha/d\theta)$ versus α (Figure 9d) was then used as an experimental master plot to describe the rate behavior of the crystal growth process based on the kinetic relationship expressed in eq 9:^{69,70,88}

$$\frac{d\alpha}{d\theta} = Af(\alpha) \quad (9)$$

The experimental master plot in differential form reveals that the growth rate decelerates over the entire course of the crystal growth process and fits the $\text{JMA}(m)$ model function with $m = 0.68 \pm 0.01$ and $A = (6.20 \pm 0.03) \times 10^{11} \text{ s}^{-1}$. When the linear rate for crystal growth from preexisting nuclei is controlled by diffusion, the kinetic exponent in the $\text{JMA}(m)$ model corresponds to one-half of the growth dimension;^{82–85} therefore, the dimension for crystal growth of SnO_2 in the present study is expected to be 1.36 based on the results of the formal kinetic analysis.

The above formal kinetic analysis based on an ideal single-step kinetic process does not necessarily provide satisfactory results. For instance, the systematic decrease in the calculated E_a values in the early stage of SnO_2 crystal growth corresponds to the range in which crystal growth accelerates under linearly increasing temperature conditions (increasing portion of the DSC exothermic peak). Furthermore, the formal kinetic analysis predicts a lower growth dimension (1.36), while the morphological observations reveal the development of a stacking structure and growth of platelike grains (two-dimensional growth) on the surface of product agglomerates of the SnO_2 product (Figure 5f). Thus, the consideration of a more complex crystal growth process is needed to account for the discrepancies between the results of formal kinetic analysis and actual kinetic process.

To interpret the actual kinetic behavior for the SnO_2 crystal growth in further detail, empirical kinetic deconvolution, which was applied to the mass-change process, was examined. Given the α range accompanied by the systematic decrease in the E_a values and the α values at the peaks of the DSC curves, two overlapping independent processes with the contributions (c_1, c_2) = (0.30, 0.70) were assumed. Average E_a values in the ranges of $0.01 \leq \alpha \leq 0.30$ and $0.30 \leq \alpha \leq 0.99$ of 201.5 and $190.5 \text{ kJ mol}^{-1}$ determined from the results of the Friedman plots (Figure 9) were adopted as the initial $E_{a,i}$ values for the first and second processes, respectively. After assuming the first-order rate equation, $\text{SB}(0,1,0)$, for $f_i(\alpha_i)$ in both of the processes, the order of each initial A_i value was determined by graphically comparing the experimental and calculated (according to eq 5) curves. The results obtained with all of the kinetic parameters optimized are shown in Figure 10. The

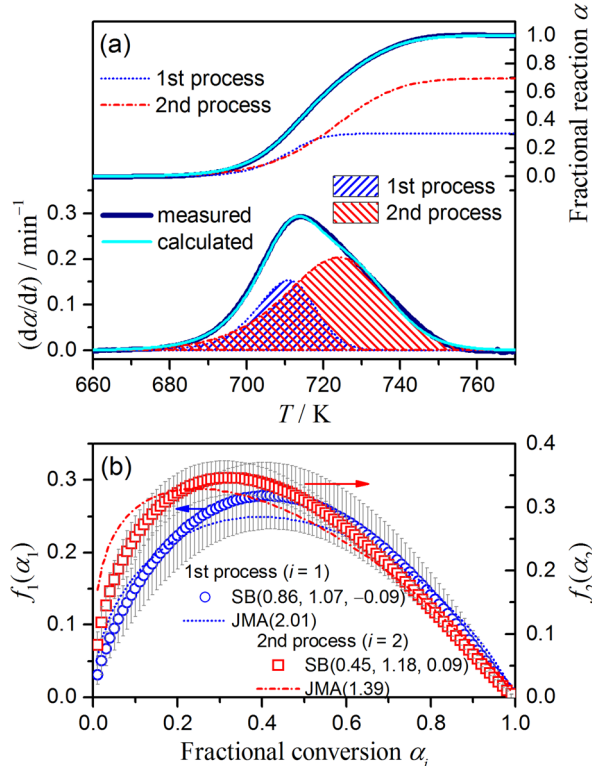


Figure 10. Results of kinetic deconvolution analysis for SnO_2 crystal growth: (a) typical results as exemplified by kinetic rate data at $\beta = 10 \text{ K min}^{-1}$ and (b) separated experimental master plots of $f_i(\alpha_i)$ versus α_i and fittings using $\text{JMA}(m)$ functions.

graphical representation of the kinetic deconvolution results (Figure 10a) indicates that two growth processes are simultaneously initiated at the beginning of crystal growth. Furthermore, during the early phase of crystal growth until the overall growth rate reaches a maximum, the two processes contribute nearly equally to the overall growth rate. The overall growth rate then decelerates because of the deceleration of the first process, and the contribution of the second process gradually increases. The first process terminates at approximately $\alpha = 0.8$; thus, the second process dominates the latter stage of crystal growth. The overlapping behavior of the two processes estimated by the empirical kinetic deconvolution analysis explains well the apparent α -dependent variation of the E_a values determined using the Friedman method (Figure 9c): the systematic decrease in E_a in the early phase during which the two processes contribute equally ($\alpha \leq 0.3$); the slightly convexed variation of E_a in the middle phase during which the contribution of the second process gradually increases ($0.30 \leq \alpha \leq 0.80$); and the slight but detectable decrease in E_a in the final phase during which the second process dominates ($\alpha \geq 0.80$). Table 2 lists the averages of the optimized kinetic parameters for the kinetic rate data at different β . The sufficiently small standard deviations of these average kinetic parameters indicate the independence of the kinetic behavior with respect to β within the range applied in the present study.

Notably, the $E_{a,1}$ value is slightly larger than $E_{a,2}$, whereas the A_1 value is larger by 1 order of magnitude than A_2 . The fact that the first process occurs in a lower-temperature region is reflected in the compensation of the larger $E_{a,1}$ by the larger A_1 .^{90,91}

The rate behaviors illustrated by the experimental master plots of the optimized $f_i(\alpha_i)$ versus α_i are largely different for the two growth processes (Figure 9d), but both of the plots indicate that the maximum rate occurs midway through the crystal growth process, as is expected for the $\text{JMA}(m)$ with $m > 1$. The best fittings of the experimental master plots with the $\text{JMA}(m)$ model are obtained with m values of 2.01 ± 0.06 and 1.39 ± 0.03 for the first and second processes, respectively. Although the fittings are not necessarily perfect, the kinetic exponent $m \approx 2$ determined for the first process is in agreement with the growth dimension for the formation of platelike grains, as was observed on the surfaces of the product agglomerates, assuming a linear growth controlled by a chemical process. Different interpretations of the slightly smaller m value estimated for the second process are possible.^{82–85} If a diffusion-controlled linear growth rate is assumed, the m value indicates a nearly three-dimensional growth process resulting in cubic or spherical crystals. On the other hand, if a chemical process-controlled linear growth rate is assumed, the prolonged platelike crystals in a specific crystallographic direction is expected. No clear morphological evidence for the formation of cubic, spherical, or prolonged platelike crystals was obtained via SEM observations of the product agglomerates (Figure 5f). If the platelike crystals were predominantly produced independent of the surface and interior structures of the product agglomerates, the nonintegral kinetic exponent, 1.39, can be explained by an intermediate rate behavior for linear growth that falls between those controlled by chemical and diffusion processes. In the present status of the physical and chemical characterization of the crystal growth process, only the growth of the XRD peaks of SnO_2 (Figure 4) and the apparent change in the surface morphology of the reactant agglomerates (Figure 5) are correlated as experimental evidence of the crystal growth to the DSC exothermic peak observed after completion of the mass-change process. Further detailed characterization of the physical and chemical natures of the crystal growth process is necessary to interpret the kinetic behavior but has not yet been possible because of difficulties with in situ observation of the agglomerate interiors during the crystal growth process. Even so, the present kinetic analysis indicates that the crystal growth of the as-produced SnO_2 can be effectively described by the occurrence of two concurrent processes characterized by different kinetic behaviors.

4. CONCLUSIONS

To achieve successful control of the reaction process and morphology of SnO_2 prepared via the direct thermal treatment of tin(II) oxyhydroxide in air, the characteristics of the thermal behavior of the dried gel-like $\text{Sn}_6\text{O}_4(\text{OH})_4$ agglomerates must be understood from two perspectives. First, the thermal dehydration-decomposition and the oxidation of the as-

Table 2. Average Kinetic Parameters for First and Second SnO_2 Crystal Growth Processes at Different β

i	c_i	$E_{a,i}$ (kJ mol $^{-1}$)	A_i (s $^{-1}$)	m_i	n_i	p_i
1	0.30 ± 0.01	197.3 ± 1.2	$(1.04 \pm 0.06) \times 10^{13}$	0.86 ± 0.02	1.07 ± 0.01	-0.09 ± 0.02
2	0.70 ± 0.01	191.1 ± 0.5	$(1.01 \pm 0.04) \times 10^{12}$	0.45 ± 0.01	1.18 ± 0.01	0.09 ± 0.01

produced intermediate SnO occur by overlapping largely during the overall mass-change process. The kinetics of both the primary thermal dehydration–decomposition process and subsequent oxidation of as-produced SnO decelerate processes, indicating similar rate behaviors, but with different E_a values. The kinetic behavior of the overall mass-change process is explained by the overlapping structure of the surface product layers formed during the thermal dehydration–decomposition and oxidation processes. Diffusional H₂O removal and O₂ intake through the surface product layers were found to play important roles in regulating the overall reaction kinetics based on the kinetic behaviors of the respective dehydration–decomposition and oxidation processes. In particular, counter-diffusion of H₂O and O₂ through the outer SnO₂ surface product layer is necessary to advance the overall reaction. Because the mass-change process is regulated by geometrical features, the size of the reactant agglomerates is a primary factor determining the kinetics of the overall mass-change process. It must also be noted that the oxidation process is significantly exothermic; therefore, under conditions that promote oxidation, the overall reaction rate is largely influenced by the self-heating effect. These statements are supported by our observations in the preliminary experiments for this study that, when using smaller agglomerates and larger sample masses and applying heating rates that are faster than those discussed herein, the reaction exhibited significant thermal runaway behavior, and the samples exploded from the sample crucible, likely due to the rapid escape of H₂O generated during the thermal dehydration–decomposition. The crystal growth of SnO₂ at higher temperatures after completion of the mass-change process also exhibited characteristic thermal behavior that was described by two concurrent kinetic processes. The two-dimensional structure of the SnO₂ product was further developed because of this behavior. Therefore, the choice of calcination temperature, which determines the crystal growth kinetics, is another important factor for controlling the SnO₂ crystallite size and the morphology of the product agglomerates.

AUTHOR INFORMATION

Corresponding Author

*Tel./fax: +81-82-424-7092. E-mail: nkoga@hiroshima-u.ac.jp.

Notes

The authors declare no competing financial interest.

ACKNOWLEDGMENTS

The present work was supported by JSPS KAKENHI Grants 25242015, 252350202, and 252350203.

REFERENCES

- Wang, H.; Rogach, A. L. Hierarchical SnO₂ Nanostructures: Recent Advances in Design, Synthesis, and Applications. *Chem. Mater.* **2014**, *26*, 123–133.
- Batzill, M.; Diebold, U. The Surface and Materials Science of Tin Oxide. *Prog. Surf. Sci.* **2005**, *79*, 47–154.
- Wang, C. C.; Akbar, S. A.; Madou, M. J. Ceramic Based Resistive Sensors. *J. Electroceram.* **1998**, *2*, 273–282.
- Jiang, L.-Y.; Wu, X.-L.; Guo, Y.-G.; Wan, L.-J. SnO₂-Based Hierarchical Nanomicrostructures: Facile Synthesis and Their Applications in Gas Sensors and Lithium-Ion Batteries. *J. Phys. Chem. C* **2009**, *113*, 14213–14219.
- Chen, H. T.; Xiong, S. J.; Wu, X. L.; Zhu, J.; Shen, J. C.; Chu, P. K. Tin Oxide Nanoribbons with Vacancy Structures in Luminescence-Sensitive Oxygen Sensing. *Nano Lett.* **2009**, *9*, 1926–1931.
- Wang, H.; Liang, Q.; Wang, W.; An, Y.; Li, J.; Guo, L. Preparation of Flower-Like SnO₂ Nanostructures and Their Applications in Gas-Sensing and Lithium Storage. *Cryst. Growth Des.* **2011**, *11*, 2942–2947.
- Shim, Y.-S.; Moon, H. G.; Kim, D. H.; Jang, H. W.; Kang, C.-Y.; Yoon, Y. S.; Yoon, S.-J. Transparent Conducting Oxide Electrodes for Novel Metal Oxide Gas Sensors. *Sens. Actuators, B* **2011**, *160*, 357–363.
- Sharma, A.; Tomar, M.; Gupta, V. Room Temperature Trace Level Detection of NO₂ Gas Using SnO₂ Modified Carbon Nanotubes Based Sensor. *J. Mater. Chem.* **2012**, *22*, 23608–23616.
- Suematsu, K.; Shin, Y.; Hua, Z.; Yoshida, K.; Yuasa, M.; Kida, T.; Shimane, K. Nanoparticle Cluster Gas Sensor: Controlled Clustering of SnO₂ Nanoparticles for Highly Sensitive Toluene Detection. *ACS Appl. Mater. Interfaces* **2014**, *6*, 5319–5326.
- Idota, Y. Tin-Based Amorphous Oxide: A High-Capacity Lithium-Ion-Storage Material. *Science* **1997**, *276*, 1395–1397.
- Zhu, J. J.; Lu, Z. H.; Aruna, S. T.; Aurbach, D.; Gedanken, A. Sonochemical Synthesis of SnO₂ Nanoparticles and Their Preliminary Study as Li Insertion Electrodes. *Chem. Mater.* **2000**, *12*, 2557–2566.
- Yang, R.; Gu, Y.; Li, Y.; Zheng, J.; Li, X. Self-Assembled 3-D Flower-Shaped SnO₂ Nanostructures with Improved Electrochemical Performance for Lithium Storage. *Acta Mater.* **2010**, *58*, 866–874.
- Wang, F.; Yao, G.; Xu, M.; Zhao, M.; Sun, Z.; Song, X. Large-Scale Synthesis of Macroporous SnO₂ with/without Carbon and Their Application as Anode Materials for Lithium-Ion Batteries. *J. Alloys Compd.* **2011**, *509*, 5969–5973.
- Wang, J.; Du, N.; Zhang, H.; Yu, J.; Yang, D. Large-Scale Synthesis of SnO₂ Nanotube Arrays as High-Performance Anode Materials of Li-Ion Batteries. *J. Phys. Chem. C* **2011**, *115*, 11302–11305.
- Bhaskar, A.; Deepa, M.; Ramakrishna, M.; Rao, T. N. Poly(3,4-Ethylenedioxothiophene) Sheath over a SnO₂ Hollow Spheres/Graphene Oxide Hybrid for a Durable Anode in Li-Ion Batteries. *J. Phys. Chem. C* **2014**, *118*, 7296–7306.
- Chen, J. S.; Ng, M. F.; Wu, H. B.; Zhang, L.; Lou, X. W. Synthesis of Phase-Pure SnO₂ Nanosheets with Different Organized Structures and Their Lithium Storage Properties. *CrystEngComm* **2012**, *14*, 5133–5136.
- Olivi, P.; Pereira, E. C.; Longo, E.; Varella, J. A.; Bulhoes, L. O. D. Preparation and Characterization of a Dip-Coated SnO₂ Film for Transparent Electrodes for Transmissive Electrochromic Devices. *J. Electrochem. Soc.* **1993**, *140*, L81–L82.
- Okuya, M.; Kaneko, S.; Hiroshima, K.; Yagi, I.; Murakami, K. Low Temperature Deposition of SnO₂ Thin Films as Transparent Electrodes by Spray Pyrolysis of Tetra-N-Butyltin(IV). *J. Eur. Ceram. Soc.* **2001**, *21*, 2099–2102.
- Fukano, T.; Motohiro, T. Low-Temperature Growth of Highly Crystallized Transparent Conductive Fluorine-Doped Tin Oxide Films by Intermittent Spray Pyrolysis Deposition. *Sol. Energy Mater. Sol. Cells* **2004**, *82*, 567–575.
- Liu, J.; Luo, T.; Mouli, T. S.; Meng, F.; Sun, B.; Li, M.; Liu, J. A Novel Coral-Like Porous SnO₂ Hollow Architecture: Biomimetic Swallowing Growth Mechanism and Enhanced Photovoltaic Property for Dye-Sensitized Solar Cell Application. *Chem. Commun.* **2010**, *46*, 472–474.
- Gu, F.; Wang, S. F.; Lu, M. K.; Zhou, G. J.; Xu, D.; Yuan, D. R. Photoluminescence Properties of SnO₂ Nanoparticles Synthesized by Sol-Gel Method. *J. Phys. Chem. B* **2004**, *108*, 8119–8123.
- Kar, A.; Kundu, S.; Patra, A. Surface Defect-Related Luminescence Properties of SnO₂ Nanorods and Nanoparticles. *J. Phys. Chem. C* **2011**, *115*, 118–124.
- Teh, J. J.; Ting, S. L.; Leong, K. C.; Li, J.; Chen, P. Gallium-Doped Tin Oxide Nano-Cuboids for Improved Dye Sensitized Solar Cell. *ACS Appl. Mater. Interfaces* **2013**, *5*, 11377–11382.
- Dou, X.; Sabba, D.; Mathews, N.; Wong, L. H.; Lam, Y. M.; Mhaisalkar, S. Hydrothermal Synthesis of High Electron Mobility Zn-Doped SnO₂ Nanoflowers as Photoanode Material for Efficient Dye-Sensitized Solar Cells. *Chem. Mater.* **2011**, *23*, 3938–3945.

- (25) Mazumder, N.; Sen, D.; Saha, S.; Ghorai, U. K.; Das, N. S.; Chattopadhyay, K. K. Enhanced Ultraviolet Emission from Mg Doped SnO_2 Nanocrystals at Room Temperature and Its Modulation Upon H_2 Annealing. *J. Phys. Chem. C* **2013**, *117*, 6454–6461.
- (26) Cavaliere, S.; Subianto, S.; Savych, I.; Tillard, M.; Jones, D. J.; Rozière, J. Dopant-Driven Nanostructured Loose-Tube SnO_2 Architectures: Alternative Electrocatalyst Supports for Proton Exchange Membrane Fuel Cells. *J. Phys. Chem. C* **2013**, *117*, 18298–18307.
- (27) Wang, W. W.; Zhu, Y. J.; Yang, L. X. ZnO-SnO_2 Hollow Spheres and Hierarchical Nanosheets: Hydrothermal Preparation, Formation Mechanism, and Photocatalytic Properties. *Adv. Funct. Mater.* **2007**, *17*, 59–64.
- (28) Sangami, G.; Dharmaraj, N. UV-Visible Spectroscopic Estimation of Photodegradation of Rhodamine-B Dye Using Tin(IV) Oxide Nanoparticles. *Spectrochim. Acta, Part A* **2012**, *97*, 847–852.
- (29) Sain, S.; Kar, A.; Patra, A.; Pradhan, S. K. Structural Interpretation of SnO_2 Nanocrystals of Different Morphologies Synthesized by Microwave Irradiation and Hydrothermal Methods. *CrystEngComm* **2014**, *16*, 1079–1090.
- (30) Xu, C. K.; Xu, G. D.; Liu, Y. K.; Zhao, X. L.; Wang, G. H. Preparation and Characterization of SnO_2 Nanorods by Thermal Decomposition of SnC_2O_4 Precursor. *Scr. Mater.* **2002**, *46*, 789–794.
- (31) Xu, C. K.; Zhao, X. L.; Liu, S.; Wang, G. H. Large-Scale Synthesis of Rutile SnO_2 Nanorods. *Solid State Commun.* **2003**, *125*, 301–304.
- (32) Kim, K.-W.; Cho, P.-S.; Lee, J.-H.; Hong, S.-H. Preparation of SnO_2 Whiskers via the Decomposition of Tin Oxalate. *J. Electroceram.* **2006**, *17*, 895–898.
- (33) Sun, H.; Kang, S.-Z.; Mu, J. Synthesis of Flowerlike SnO_2 Quasi-Square Submicrotubes from Tin (II) Oxalate Precursor. *Mater. Lett.* **2007**, *61*, 4121–4123.
- (34) Taib, H.; Sorrell, C. C. Preparation of Tin Oxide. *J. Aust. Ceram. Soc.* **2007**, *43*, 56–61.
- (35) Taib, H.; Sorrella, C. C. Assessment of Particle Sizing Methods Applied to Agglomerated Nanoscale Tin Oxide (SnO_2). *J. Aust. Ceram. Soc.* **2008**, *44*, 47–51.
- (36) Szirtes, L.; Megyeri, J.; Kuzmann, E. Thermal Treatment on Tin(II/IV) Oxalate, EDTA and Sodium Inositol-Hexaphosphate. *J. Therm. Anal. Calorim.* **2012**, *107*, 1225–1230.
- (37) Wang, Q. H.; Wang, D. W.; Wang, T. M. Shape-Controlled Synthesis of Porous SnO_2 Nanostructures via Morphologically Conserved Transformation from SnC_2O_4 Precursor Approach. *Nano-Micro Lett.* **2011**, *3*, 34–42.
- (38) Wang, X.; Zhao, C.; Liu, R.; Liu, X.; Shen, Q. Preparation and Comparative Structural Properties of Porous SnO_2 Microrods and Submicrorods. *Ionics* **2014**, *20*, 841–848.
- (39) Galwey, A. K.; Brown, M. E. *Thermal Decomposition of Ionic Solids*; Elsevier: Amsterdam, 1999.
- (40) Galwey, A. K. Structure and Order in Thermal Dehydrations of Crystalline Solids. *Thermochim. Acta* **2000**, *355*, 181–238.
- (41) Koga, N.; Tanaka, H. A Physico-Geometric Approach to the Kinetics of Solid-State Reactions as Exemplified by the Thermal Dehydration and Decomposition of Inorganic Solids. *Thermochim. Acta* **2002**, *388*, 41–61.
- (42) Kitabayashi, S.; Koga, N. Physico-Geometrical Mechanism and Overall Kinetics of Thermally Induced Oxidative Decomposition of Tin(II) Oxalate in Air: Formation Process of Microstructural Tin(IV) Oxide. *J. Phys. Chem. C* **2014**, *118*, 17847–17861.
- (43) Wang, Y.-F.; Li, K.-N.; Liang, C.-L.; Hou, Y.-F.; Su, C.-Y.; Kuang, D.-B. Synthesis of Hierarchical SnO_2 Octahedra with Tailorable Size and Application in Dye-Sensitized Solar Cells with Enhanced Power Conversion Efficiency. *J. Mater. Chem.* **2012**, *22*, 21495.
- (44) Khanderi, J.; Shi, L.; Rothenberger, A. Hydrolysis of Bis(Dimethylamido)Tin to Tin (II) Oxyhydroxide and Its Selective Transformation into Tin (II) or Tin (IV) Oxide. *Inorg. Chim. Acta* **2015**, *427*, 27–32.
- (45) Koga, N.; Goshi, Y.; Yamada, S.; Pérez-Maqueda, L. A. Kinetic Approach to Partially Overlapped Thermal Decomposition Processes. *J. Therm. Anal. Calorim.* **2013**, *111*, 1463–1474.
- (46) Abrahams, I.; Grimes, S. M.; Johnston, S. R.; Knowles, J. C. Tin(II) Oxyhydroxide by X-Ray Powder Diffraction. *Acta Crystallogr., Sect. C: Cryst. Struct. Commun.* **1996**, *52*, 286–288.
- (47) Zhao, B.; Shao, G.; Fan, B.; Wang, C.; Xie, Y.; Zhang, R. Preparation and Enhanced Microwave Absorption Properties of Ni Microspheres Coated with $\text{Sn}_6\text{O}_4(\text{OH})_4$ Nanoshells. *Powder Technol.* **2015**, *270*, 20–26.
- (48) Okamura, K.; Nasr, B.; Brand, R. A.; Hahn, H. Solution-Processed Oxide Semiconductor SnO in P-Channel Thin-Film Transistors. *J. Mater. Chem.* **2012**, *22*, 4607–4610.
- (49) Choi, W. K.; Sung, H.; Kim, K. H.; Cho, J. S.; Choi, S. C.; Jung, H. J.; Koh, S. K.; Lee, C. M.; Jeong, K. Oxidation Process from SnO to SnO_2 . *J. Mater. Sci. Lett.* **1997**, *16*, 1551–1554.
- (50) Baur, W. H. Über Die Verfeinerung Der Kristallstrukturbestimmung Einiger Vertreter Des Rutiltyps: TiO_2 , SnO_2 , GeO_2 und MgF_2 . *Acta Crystallogr.* **1956**, *9*, 515–520.
- (51) Patterson, A. The Scherrer Formula for X-Ray Particle Size Determination. *Phys. Rev.* **1939**, *56*, 978–982.
- (52) Uchiyama, H.; Imai, H. Tin Oxide Meshes Consisting of Nanoribbons Prepared through an Intermediate Phase in an Aqueous Solution. *Cryst. Growth Des.* **2007**, *7*, 841–843.
- (53) Noda, Y.; Koga, N. Phenomenological Kinetics of the Carbonation Reaction of Lithium Hydroxide Monohydrate: Role of Surface Product Layer and Possible Existence of a Liquid Phase. *J. Phys. Chem. C* **2014**, *118*, 5424–5436.
- (54) Sánchez-Jiménez, P. E.; Perejón, A.; Criado, J. M.; Diánez, M. J.; Pérez-Maqueda, L. A. Kinetic Model for Thermal Dehydrochlorination of Poly(Vinyl Chloride). *Polymer* **2010**, *51*, 3998–4007.
- (55) Perejón, A.; Sánchez-Jiménez, P. E.; Criado, J. M.; Pérez-Maqueda, L. A. Kinetic Analysis of Complex Solid-State Reactions. A New Deconvolution Procedure. *J. Phys. Chem. B* **2011**, *115*, 1780–1791.
- (56) Koga, N.; Suzuki, Y.; Tatsuoka, T. Thermal Dehydration of Magnesium Acetate Tetrahydrate: Formation and in Situ Crystallization of Anhydrous Glass. *J. Phys. Chem. B* **2012**, *116*, 14477–14486.
- (57) Sánchez-Jiménez, P. E.; Pérez-Maqueda, L. A.; Perejón, A.; Criado, J. M. Nanoclay Nucleation Effect in the Thermal Stabilization of a Polymer Nanocomposite: A Kinetic Mechanism Change. *J. Phys. Chem. C* **2012**, *116*, 11797–11807.
- (58) Koga, N.; Yamada, S.; Kimura, T. Thermal Decomposition of Silver Carbonate: Phenomenology and Physicogeometrical Kinetics. *J. Phys. Chem. C* **2013**, *117*, 326–336.
- (59) Wada, T.; Koga, N. Kinetics and Mechanism of the Thermal Decomposition of Sodium Percarbonate: Role of the Surface Product Layer. *J. Phys. Chem. A* **2013**, *117*, 1880–1889.
- (60) Koga, N.; Kasahara, D.; Kimura, T. Aragonite Crystal Growth and Solid-State Aragonite–Calcite Transformation: A Physico-Geometrical Relationship via Thermal Dehydration of Included Water. *Cryst. Growth Des.* **2013**, *13*, 2238–2246.
- (61) Svoboda, R.; Málek, J. Applicability of Fraser–Suzuki Function in Kinetic Analysis of Complex Crystallization Processes. *J. Therm. Anal. Calorim.* **2013**, *111*, 1045–1056.
- (62) Koga, N.; Nishikawa, K. Mutual Relationship between Solid-State Aragonite–Calcite Transformation and Thermal Dehydration of Included Water in Coral Aragonite. *Cryst. Growth Des.* **2014**, *14*, 879–887.
- (63) Yoshikawa, M.; Yamada, S.; Koga, N. Phenomenological Interpretation of the Multistep Thermal Decomposition of Silver Carbonate to Form Silver Metal. *J. Phys. Chem. C* **2014**, *118*, 8059–8070.
- (64) Yoshikawa, M.; Goshi, Y.; Yamada, S.; Koga, N. Multistep Kinetic Behavior in the Thermal Degradation of Poly(L-Lactic Acid): A Physico-Geometrical Kinetic Interpretation. *J. Phys. Chem. B* **2014**, *118*, 11397–11405.

- (65) Perejón, A.; Sánchez-Jiménez, P. E.; Criado, J. M.; Pérez-Maqueda, L. A. Thermal Stability of Multiferroic BiFeO₃: Kinetic Nature of the β - γ Transition and Peritectic Decomposition. *J. Phys. Chem. C* **2014**, *118*, 26387–26395.
- (66) Kikuchi, S.; Koga, N.; Seino, H.; Ohno, S. Kinetic Study on Liquid Sodium–Silica Reaction for Safety Assessment of Sodium-Cooled Fast Reactor. *J. Therm. Anal. Calorim.* **2015**, *121*, 45–55.
- (67) Ogasawara, H.; Koga, N. Kinetic Modeling for Thermal Dehydration of Ferrous Oxalate Dihydrate Polymorphs: A Combined Model for Induction Period-Surface Reaction-Phase Boundary Reaction. *J. Phys. Chem. A* **2014**, *118*, 2401–2412.
- (68) Koga, N.; Šesták, J.; Simon, P. Some Fundamental and Historical Aspects of Phenomenological Kinetics in the Solid State Studied by Thermal Analysis. In *Thermal Analysis of Micro, Nano- and Non-Crystalline Materials*; Šesták, J., Simon, P., Eds.; Springer: Dordrecht, The Netherlands 2013; pp 1–28.
- (69) Koga, N. Ozawa's Kinetic Method for Analyzing Thermoanalytical Curves. *J. Therm. Anal. Calorim.* **2013**, *113*, 1527–1541.
- (70) Ozawa, T. A New Method of Analyzing Thermogravimetric Data. *Bull. Chem. Soc. Jpn.* **1965**, *38*, 1881–1886.
- (71) Doyle, C. D. Series Approximations to the Equation of Thermogravimetric Data. *Nature* **1965**, *207*, 290–291.
- (72) Kissinger, H. E. Reaction Kinetics in Differential Thermal Analysis. *Anal. Chem.* **1957**, *29*, 1702–1706.
- (73) Šesták, J.; Berggren, G. Study of the Kinetics of the Mechanism of Solid-State Reactions at Increasing Temperatures. *Thermochim. Acta* **1971**, *3*, 1–12.
- (74) Šesták, J. Diagnostic Limits of Phenomenological Kinetic Models Introducing the Accommodation Function. *J. Therm. Anal.* **1990**, *36*, 1997–2007.
- (75) Šesták, J. Rationale and Fallacy of Thermoanalytical Kinetic Patterns. *J. Therm. Anal. Calorim.* **2012**, *110*, 5–16.
- (76) Málek, J.; Criado, J. M. Empirical Kinetic Models in Thermal Analysis. *Thermochim. Acta* **1992**, *203*, 25–30.
- (77) Pérez-Maqueda, L. A.; Criado, J. M.; Sánchez-Jiménez, P. E. Combined Kinetic Analysis of Solid-State Reactions: A Powerful Tool for the Simultaneous Determination of Kinetic Parameters and the Kinetic Model without Previous Assumptions on the Reaction Mechanism. *J. Phys. Chem. A* **2006**, *110*, 12456–12462.
- (78) Koga, N.; Kimizu, T. Thermal Decomposition of Indium(III) Hydroxide Prepared by the Microwave-Assisted Hydrothermal Method. *J. Am. Ceram. Soc.* **2008**, *91*, 4052–4058.
- (79) Koga, N.; Mako, A.; Kimizu, T.; Tanaka, Y. Thermal Decomposition of Synthetic Antlerite Prepared by Microwave-Assisted Hydrothermal Method. *Thermochim. Acta* **2008**, *467*, 11–19.
- (80) Gotor, F. J.; Criado, J. M.; Málek, J.; Koga, N. Kinetic Analysis of Solid-State Reactions: The Universality of Master Plots for Analyzing Isothermal and Nonisothermal Experiments. *J. Phys. Chem. A* **2000**, *104*, 10777–10782.
- (81) Criado, J. M.; Pérez-Maqueda, L. A.; Gotor, F. J.; Málek, J.; Koga, N. A Unified Theory for the Kinetic Analysis of Solid State Reactions under Any Thermal Pathway. *J. Therm. Anal. Calorim.* **2003**, *72*, 901–906.
- (82) Avrami, M. Kinetics of Phase Change. I. General Theory. *J. Chem. Phys.* **1939**, *7*, 1103–1112.
- (83) Avrami, M. Kinetics of Phase Change. II. Transformation-Time Relations for Random Distribution of Nuclei. *J. Chem. Phys.* **1940**, *8*, 212–223.
- (84) Avrami, M. Kinetics of Phase Change. III. Granulation, Phase Change, and Microstructure. *J. Chem. Phys.* **1941**, *9*, 177–184.
- (85) Barmak, K. A Commentary On: “Reaction Kinetics in Processes of Nucleation and Growth. *Metall. Mater. Trans. A* **2010**, *41*, 2711–2775.
- (86) Friedman, H. L. Kinetics of Thermal Degradation of Cha-Forming Plastics from Thermogravimetry, Application to a Phenolic Plastic. *J. Polym. Sci., Part C: Polym. Symp.* **1964**, *6*, 183–195.
- (87) Ozawa, T. Applicability of Friedman Plot. *J. Therm. Anal.* **1986**, *31*, 547–551.
- (88) Koga, N. Kinetic Analysis of Thermoanalytical Data by Extrapolating to Infinite Temperature. *Thermochim. Acta* **1995**, *258*, 145–159.
- (89) Ozawa, T. Non-Isothermal Kinetics and Generalized Time. *Thermochim. Acta* **1986**, *100*, 109–118.
- (90) Koga, N.; Šesták, J. Kinetic Compensation Effect as a Mathematical Consequence of the Exponential Rate-Constant. *Thermochim. Acta* **1991**, *182*, 201–208.
- (91) Koga, N. A Review of the Mutual Dependence of Arrhenius Parameters Evaluated by the Thermoanalytical Study of Solid-State Reactions: The Kinetic Compensation Effect. *Thermochim. Acta* **1994**, *244*, 1–20.